Earthquake Stress Drop for a Circular Crack in an Anisotropic Medium

Shuhang Tang[*1,2], Yingcai Zheng[2], Hua-Wei Zhou[2], and Hao Hu[2]

ABSTRACT

The circular-crack model has been widely used in seismology to infer earthquake stress drop. A common assumption is that the background medium is isotropic, although many earthquakes occur in geologically anisotropic settings. In this article, we study the effect of anisotropy on stress drop for a circular crack model and present explicit formalism in both static and kinematic cases. In the static case, we obtain the relationship between stress drop and slip for a circular crack model in an arbitrarily anisotropic medium. Special attention is given to the transversely isotropic (TI) medium. The static formalism is useful in understanding stress drop, but not all quantities are observables. Therefore, we resort to the kinematic case, from which we can infer stress drop using recorded far-field body waves. In the kinematic case, we assume that the crack ruptures circularly and reaches the final displacement determined by the static solutions. The far-field waveforms show that the corner frequency will change with different anisotropic parameters. Finally, we calculate the stress drops for cracks in isotropic and anisotropic media using the far-field waveforms. We find that in an isotropic medium, only shear stress acting on the crack surface contributes to shear slip. However, in a TI medium, if the anisotropy symmetry axis is not perpendicular or parallel to the crack surface, a normal stress (normal to the crack surface) can produce a shear slip. In calculating stress drop for an earthquake in an anisotropic medium using far-field body waves, a large error may be introduced if we ignore the possible anisotropy in the inversion. For a TI medium with about 18% anisotropy, the misfit of inferred stress drop could be up to 41%. Considering the anisotropic information, we can further improve the accuracy of stress-drop inversion.

KEY POINTS

- We study the circular crack model in anisotropic media for static and kinematic cases.
- The inferred stress drop could have a 41% misfit for a medium with 18% anisotropy using the isotropic formula.
- Inverting stress drop should consider the background medium anisotropy if possible.

Supplemental Material

INTRODUCTION

Stress drop is among the most critical parameters of earthquakes (Kanamori and Brodsky, 2004). A constant stress drop gives the theoretical basis of the scaling law in seismology (Kanamori and Anderson, 1975; Lin *et al.*, 2012; Cocco *et al.*, 2016). Stress drop is also used to model ground motion (Hanks and Mcguire, 1981; Hutchings, 1994; Mavroeidis *et al.*, 2008). Researchers use the circular crack model to calculate stress drop (Oncescu, 1986; Zollo *et al.*, 2014). For a circular crack, Eshelby (1957) gave a mathematical framework of the relationship among the stress drop, slip, and fault area. Brune (1970) studied a kinematic model and discovered the relationship between the fault dimension and the corner frequency of the earthquake source spectrum. Following Brune (1970), several authors have studied the kinematic and dynamic aspects of circular cracks (Sato and Hirasawa, 1973; Dahlen, 1974; Madariaga, 1976; Boatwright, 1980; Dong and Papageorgiou, 2002a; Kaneko and Shearer, 2015). Combining the static and kinematic rupture properties, Aki (1972) gave an expression of stress drop in terms of the scalar seismic moment and the corner frequency, which can be estimated from far-field body waves; this is in sharp contrast with the static estimation of the slip and fault area. Estimating earthquake stress drop is essential for studying the tectonics of different regions

1. School of Geoscience and Technology, Southwest Petroleum University, Chengdu, China, https://orcid.org/0000-0001-6463-9135 (ST); 2. Department of Earth and Atmospheric Sciences, University of Houston, Houston, Texas, U.S.A., https://orcid.org/0000-0001-9179-8940 (YZ); https://orcid.org/0000-0001-6660-5297 (H-WZ)

*Corresponding author: tshswacm@gmail.com

Cite this article as Tang, S., Y. Zheng, H.-W. Zhou, and H. Hu (2022). Earthquake Stress Drop for a Circular Crack in an Anisotropic Medium, *Bull. Seismol. Soc. Am.* **113**, 297–311, doi: 10.1785/0120220075

(Allmann and Shearer, 2007; Uchida *et al.*, 2012; Baltay *et al.*, 2013; Abercrombie, 2014) and different types of earthquakes, for example, induced earthquakes (Goertz-Allmann *et al.*, 2011; Huang *et al.*, 2016; Wu *et al.*, 2018). However, all of the aforementioned works assume seismic isotropy for the background media. Furthermore, for most studies using the circular crack model, the background media are assumed to be Poisson solids, that is, $\lambda = \mu$ (Sato and Hirasawa, 1973; Kanamori and Anderson, 1975), in which μ is the rigidity and λ is the other Lamé elastic parameter.

It is known that many earthquakes occur in anisotropic geologic settings, such as subducting slabs (Li *et al.*, 2018) and plate boundaries (Song and Kawakatsu, 2012). However, few researchers considered the seismic anisotropy when calculating stress drop. Recently, large-scale developments in the oil, gas, and water disposal industry induce seismicity in anisotropic sedimentary layers such as shale (Talebi and Boone, 1998; Sondergeld and Rai, 2011; Grechka and Yaskevich, 2013). Many factors can give rise to the seismic anisotropy of the media, such as mineralogy, alignment of inhomogeneity inclusions, fine-layering fabrics, and stress-induced anisotropy (Schoenberg and Sayers, 1995).

Our goal here is to study the circular crack model in anisotropic media for static and kinematic cases. By studying the circular crack model, we will gain deeper understanding on how anisotropy can affect the estimated stress drop of earthquakes in anisotropic media if ignoring anisotropy in the stress-drop inversion. Furthermore, we can express the formula for inverting stress drop for anisotropic media.

In this study, we follow the assumptions made by Eshelby (1957). We first derive the static equation for stress drop in a generally homogeneous but anisotropic medium using the eigenstrain given by Mura (1987). Then, we use numerical examples to show that our equation gives the same result as the equation of Eshelby (1957) in a Poisson solid (isotropic and $\lambda = \mu$). There is a significant limitation of using static solution to infer stress drop in practice. Namely, the static equation gives stress drop using the average slip (Δu) and radius of the crack (R), which are not observables. Therefore, we further study the kinematic model to infer stress drop from observable parameters such as the scalar seismic moment (M_0) and corner frequency in an anisotropic medium. For the kinematic model, we follow the recipe by Sato and Hirasawa (1973), which incorporates a kinematic rupture process into the solution for an isotropic medium, with an additional deceleration phase of rupture velocity (Boatwright 1980). We compute the far-field body waveforms and their frequency spectra, which are used to calculate stress drop for both isotropic and anisotropic media. We then discuss the influence of anisotropy on the scalar seismic moment and the radius of the crack. In inferring the crack radius, we discuss the influence of anisotropy on the measured corner frequency and its related constants (called C_P and C_S). Then, we discuss the influence of anisotropy on the stress drop.

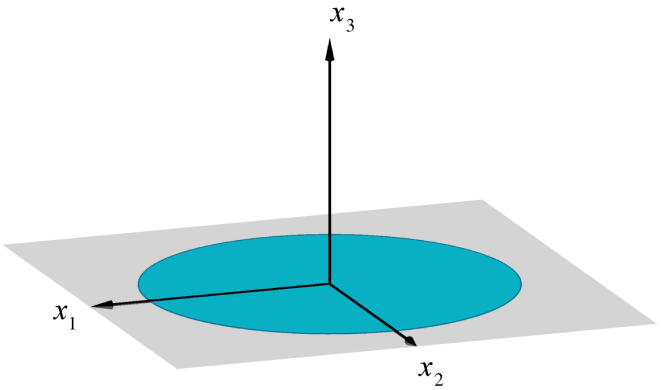

Figure 1. The coordinate system and a flat crack (blue) embedded in a homogeneous medium. The color version of this figure is available only in the electronic edition.

From both the static and kinematic models, we can estimate the amount of error of stress drop introduced by the ignorance of anisotropy.

Our contributions can be summarized in two aspects. First, we extend the procedure of inferring stress drop into anisotropic media. Second, we quantitatively analyze the errors due to the ignorance of anisotropic information in the inversion of stress drop where the background medium may be anisotropic.

THE STATIC SOLUTION FOR STRESS DROP AND SLIP

Problem statement

To estimate the effect of anisotropy on estimating stress drop, we study the anisotropic circular crack model, which relates the stress drop with slip. This model assumes that, before the earthquake, the homogeneous anisotropic background medium is continuous everywhere, and a shear stress σ_{13} acts in the far field. After the earthquake happens, a thin crack (Fig. 1) with radius R forms, and the stress on the crack surface drops to zero. Stress drop refers to this change in shear stress ($\Delta\sigma$) along the crack surface. For a flat crack, we define $\Delta\sigma = \sigma_{13}$. We would show the relationship between the stress drop $\Delta\sigma$ and the displacement discontinuity Δu, on two opposing crack surfaces.

Static stress drop of a crack in an anisotropic medium

We derive the relationship between the stress drop and slip (i.e., displacement discontinuity), defined as the relative motion between two crack surfaces, based on the concept of the eigenstrain (Eshelby, 1957; Walpole, 1977; Mura, 1987; Weinberger *et al.*, 2005).

We only show the main results subsequently. For the readers interested in the derivation, please refer to Appendix A. The slip on the crack surface is given as

$$\Delta u(r) = \frac{-2\sigma_{13}\tilde{\mathbf{L}}_{3333}}{\tilde{\mathbf{L}}_{3333}\tilde{\mathbf{L}}_{3131} - \tilde{\mathbf{L}}_{3133}\tilde{\mathbf{L}}_{3331}}\sqrt{R^2 - r^2}, \qquad (1)$$

in which σ_{13} is the applied shear stress, R is the radius of the crack, r is the distance from one point inside the crack to the center of the crack, and the tensor $\tilde{\mathbf{L}}_{ijmn}$ is defined as

$$\tilde{\mathbf{L}}_{ijmn} = -\frac{1}{4\pi}\mathbf{C}_{ijkl}\mathbf{C}_{pqmn}\Pi_{kplq}R, \tag{2}$$

in which $\mathbf{C}_{ijkl}$ is the fourth-rank elastic stiffness tensor and each subscript takes value 1, 2, or 3, and

$$\Pi_{kplq} = \int_{S^2} \frac{\mathbf{G}_{kplq}(\vec{\xi})dS(\vec{\xi})}{a_1^2a_2^2a_3^2\left(\frac{\vec{\xi}_1^2}{a_2^2a_3^2}+\frac{\vec{\xi}_2^2}{a_3^2a_1^2}+\frac{\vec{\xi}_3^2}{a_1^2a_2^2}\right)^{\frac{3}{2}}}, \tag{3}$$

in which $\mathbf{G}_{kplq}$ is a tensor (see Appendix A) in a homogeneous anisotropic medium given by Mura (1987) and $\vec{\xi}$ is the directional vector lies on a unit sphere. The a_1, a_2, and a_3 are the three semiaxis of the crack (i.e., $a_1 = a_2 = R$ and $a_3 \to 0$).

Taking the spatial average of equation (1), we get the average slip $\overline{\Delta u}$ on the crack surface:

$$\overline{\Delta u} = -\frac{4}{3}\frac{R\Delta\sigma\tilde{\mathbf{L}}_{3333}}{\tilde{\mathbf{L}}_{3333}\tilde{\mathbf{L}}_{3131}-\tilde{\mathbf{L}}_{3133}\tilde{\mathbf{L}}_{3331}}. \tag{4}$$

Using equation (4), we can estimate the static stress drop in an anisotropic medium as

$$\Delta\sigma = -\frac{3}{4}\frac{\overline{\Delta u}(\tilde{\mathbf{L}}_{3333}\tilde{\mathbf{L}}_{3131}-\tilde{\mathbf{L}}_{3133}\tilde{\mathbf{L}}_{3331})}{R\tilde{\mathbf{L}}_{3333}}. \tag{5}$$

In isotropic media, both Π_{kplq} (equation 3) and $\tilde{\mathbf{L}}_{ijmn}$ can be calculated analytically (see Appendix B). We find that for the isotropic case, $\tilde{\mathbf{L}}_{3133} = \tilde{\mathbf{L}}_{3331} = 0$, equation (5) becomes

$$\Delta\sigma = -\frac{3}{4}\frac{\overline{\Delta u}\tilde{\mathbf{L}}_{3131}}{R}, \tag{6}$$

and $\tilde{\mathbf{L}}_{3131} = -\frac{\pi\mu(3\lambda+4\mu)}{4(\lambda+2\mu)}$. For the particular case for a Poisson solid when $\lambda = \mu$, $\tilde{\mathbf{L}}_{3131} = -\frac{7\pi\mu}{12}$. In this case, equation (6) reduces to the equation of Eshelby (1957):

$$\Delta\sigma = \frac{7\pi}{16}\frac{\mu\overline{\Delta u}}{R}. \tag{7}$$

Numerical example: static stress drop in isotropic and anisotropic media

Here, we give a numerical example using equation (5) to calculate stress drop in an anisotropic medium. We assume the earthquake occurs in an anisotropic background medium with elastic properties same as the Mesaverde clayshale (Thomsen, 1986), which is vertical transversely isotropic (e.g., horizontally layered fabric with a vertical symmetry axis) with about 18% anisotropy. The crack surface (horizontal) is perpendicular to the symmetry axis of the anisotropic medium. The Mesaverde clayshale has vertically propagating P-wave velocity $V_P = 3794$ m/s, vertically propagating S-wave velocity $V_S = 2074$ m/s, density $\rho = 2560$ kg/m^3, and the Thomsen anisotropy parameters $\varepsilon = 0.189$, $\delta = 0.204$, and $\gamma = 0.175$ (Table 1). The relationship between elastic stiffness tensor $\mathbf{C}_{ijkl}$ and Thomsen parameters is given in Appendix C. We set the radius of the crack as R = 2000 m and a slip of $\overline{\Delta u} = 0.1$ m. According to equation (5), the stress drop is $\Delta\sigma = 8.99 \times 10^5$ Pa.

TABLE 1
Elastic Parameters for Mesaverde Clayshale

V_P (m/s)	V_S (m/s)	ρ (kg/m^3)	ε	δ	γ
3794	2074	2560	0.189	0.204	0.175

To study the effect of anisotropy on stress drop, we compare the stress drop, which results in the same slip but for the isotropic medium. Because equation (7) only works for a Poisson solid, we further assume the background medium has S-wave velocity $V_S = 2074$ m/s, and the medium has no anisotropy ($\varepsilon = 0$, $\delta = 0$, and $\gamma = 0$) with density $\rho = 2560$ kg/m^3. The calculated stress drop will be $\Delta\sigma = 7.57 \times 10^5$ Pa using equation (7).

Comparing the computed stress-drop values using both anisotropic and isotropic models with the same slip, we can see that the anisotropy could cause a 16% difference in the stress drop in our anisotropic model.

Numerical example: effect of crack orientation on the stress drop

The previous examples indicate that the stress drop is different in isotropic and anisotropic media for the same fault size and slip strength. In this section, we give a numerical example to show the impact of the crack orientation on the relationship between the slip and stress drop.

We show the impact of the crack orientation between stress drop and slip for two separate stress states: (1) only shear stress and (2) only normal stress applied in the far field. Here "shear" and "normal" are with respect to the crack surface. The real stress state can be a combination of these two states. We again use the Mesaverde clayshale as the anisotropic background medium. We simultaneously rotate both the crack and the applied far-field shear stress corresponding to the x_2 axis (Fig. 2) but keep the anisotropy orientation fixed. After the rotation, the crack and the stresses are no longer parallel or normal to the coordinate axis x_1. We use σ'_{13} to represent the new rotated shear stress and σ'_{33} to represent the new normal stress corresponding to the new x'_1, x'_2, and x'_3 axis (Fig. 2). We use $\overline{\Delta u}$ to represent the scalar value of the slip on the crack surface.

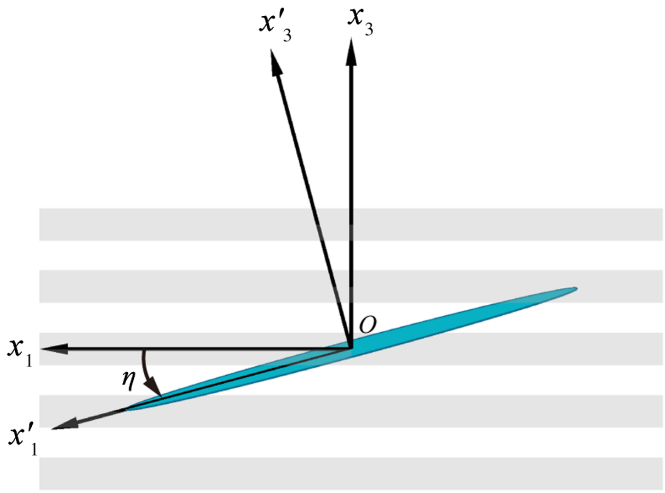

Figure 2. The 2D view of the rotation of the crack plane. η is the rotation angle (left-handed rotation about the x_2 axis) between the fault plane and the x_1 axis. x_2 axis points out of the represented plane. Gray thick lines indicate layering of the anisotropic fabric. The color version of this figure is available only in the electronic edition.

In numerical calculation, we set $\sigma'_{13} = \Delta\sigma = 8.99 \times 10^5$ Pa, and we rotate the crack by an angle η (Fig. 2). Then, we use equation (4) (i.e., anisotropic case) to calculate the slip across the crack interface (Fig. 3a) caused by the same amount of shear stress drop. We can see (Fig. 3a) that for the same amount of slip, the stress-drop difference can be about 16% between different rotation angles. The result shows that in the anisotropic medium, applying the same stress to cracks with different orientations could produce different magnitudes of slips.

In equation (4), we show the relationship between slip and shear stress. Next, we consider possible shear slip caused by an applied normal stress. The eigenstrain due to a normal stress is also given by Mura (1987). We give the equation of the shear slip caused by the normal stress (σ_{33}):

$$\overline{\Delta u} = -\frac{4}{3}\frac{R\sigma_{33}\tilde{\mathbf{L}}_{3133}}{\tilde{\mathbf{L}}_{3333}\tilde{\mathbf{L}}_{3131} - \tilde{\mathbf{L}}_{3133}\tilde{\mathbf{L}}_{3331}}. \tag{8}$$

By setting $\sigma_{33} = \Delta\sigma$, we will obtain the slip in the pure normal case (Fig. 3b). For the pure normal case, the maximum slip is about 0.01 m at an angle of $\eta = 45°$. Furthermore, our calculation shows that if the anisotropy symmetry axis is perpendicular or parallel to the crack surface for a transversely isotropic (TI) medium, the normal stress applied to the crack result in zero shear slip, which makes physical sense due to symmetry.

Comparing Figure 3a,b, we can see that to produce the same amount of shear slip across the crack interface, the magnitude of the normal stress needs to be 10 times larger than the shear stress.

The kinematic solution for stress drop and slip

In the previous static solution, we have discussed the relationship between stress drop and slip in anisotropic media. However, in reality, there are some limitations on using equation (5) to infer stress drop because the subsurface slip is not known across the fault surface. To overcome this difficulty, Aki (1972) used the following equation to infer stress drop:

$$\Delta\sigma = \frac{7M_0}{16R^3}. \tag{9}$$

In this equation, Aki (1972) used the scalar seismic moment M_0 instead of Δu and μ to calculate stress drop, in which M_0 can be inferred from observed far-field body waves. In this section, we will construct a kinematic faulting model to calculate far-field seismograms. We then use the seismic waveforms to estimate the scalar seismic moment as well as the radius of crack, and then the stress drop.

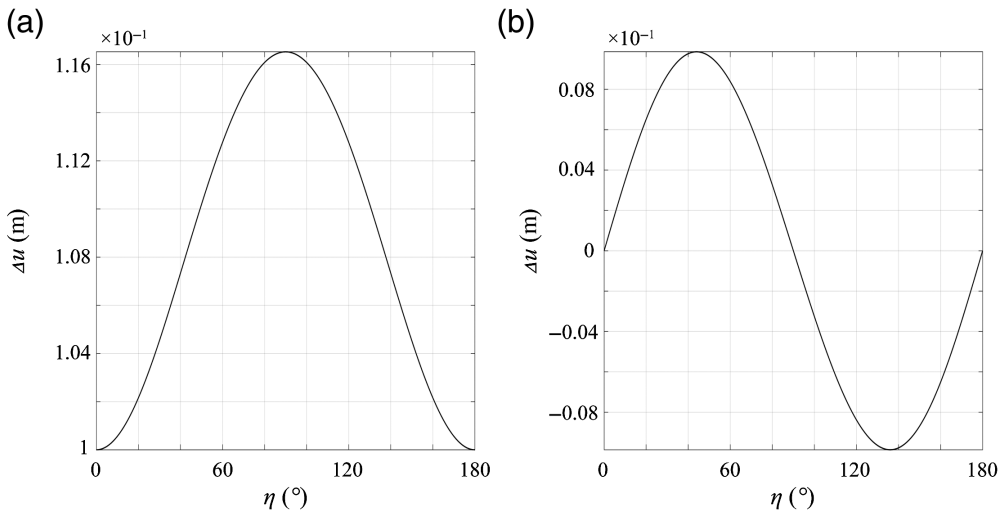

Figure 3. The slip at angles η due to the same amount of stress drop. (a) Slip caused by shear stress drop and (b) slip caused by normal stress drop.

Earthquake rupture process

The static stress drop formula can be used to construct the earthquake rupture process following Sato and Hirasawa (1973). They assume that the rupture on a circular crack initiates at the center of the

circular fault and propagates radially outward at a constant rupture velocity. The rupture stops when the crack reaches a predefined fault boundary (radius of crack as R). However, the model of Sato and Hirasawa has an unphysical feature that the slip suddenly arrested everywhere on the fault (Kaneko and Shearer, 2014; Udias *et al.*, 2014). To avoid this unphysical feature, we add a deceleration phase to the rupture process following Boatwright (1980), Dong and Papageorgiou (2002b), and Sato and Hirasawa (2009). Suppose the rupture initiates at $t = 0$ s, using equation (1), we obtain the slip function (also called source time function) across the fault surface as follows:

$$\Delta u(r,t) = \frac{-2\Delta\sigma\tilde{\mathbf{L}}_{3333}}{\tilde{\mathbf{L}}_{3333}\tilde{\mathbf{L}}_{3311} - \tilde{\mathbf{L}}_{3133}\tilde{\mathbf{L}}_{3331}}\sqrt{(vt)^2 - r^2}, \frac{r}{v} \le t \le t_s$$

$$\Delta u(r,t) = \frac{-2\Delta\sigma\tilde{\mathbf{L}}_{3333}}{\tilde{\mathbf{L}}_{3333}\tilde{\mathbf{L}}_{3311} - \tilde{\mathbf{L}}_{3133}\tilde{\mathbf{L}}_{3331}}\sqrt{(vt)^2 - \kappa(v(t-t_s))^2 - r^2}, \quad t_s < t < t_h,$$

$$\Delta u(r,t) = \frac{-2\Delta\sigma\tilde{\mathbf{L}}_{3333}}{\tilde{\mathbf{L}}_{3333}\tilde{\mathbf{L}}_{3311} - \tilde{\mathbf{L}}_{3133}\tilde{\mathbf{L}}_{3331}}\sqrt{R^2 - r^2}, t_h \le t, \qquad (10)$$

in which v is the rupture velocity, r is the distance from any point on the crack to the center of the crack, and $r \le R$ because R is the radius of the crack. The deceleration time and stop time are given by $t_s = \frac{R}{v}(\frac{\kappa-1}{\kappa})^{1/2}$ and $t_s = \frac{R}{v}(\frac{\kappa}{\kappa-1})^{1/2}$, in which κ is a parameter that determines the duration of the deceleration. We choose $\kappa = 3$ following Boatwright (1980).

To calculate the far-field displacement of the seismic wave from the rupture process, we partition the circular fault into discrete small grids. We assume that the slip at each grid follows a step-function, in which the slip on the grid remains zero until the rupture front arrives at that grid. After the rupture front arrived, the magnitude of the slip is specified by the source time function, and finally reaches the static equation (equation 1). The observed seismic field is a linear superposition of all seismic waves generated by the slip on all the grids on the circular fault, and the calculation is performed in the Cartesian system (Fig. 4).

Far-field seismic displacement due to a crack model

Following the study of Aki and Richards (2002), the seismic displacement field corresponding to the crack slip can be represented as

$$\mathbf{u}_i(\vec{\mathbf{x}},t) = \int_{-\infty}^{\infty} d\tau \iint_{\Sigma} [\mathbf{u}_j(\vec{\xi},\tau)]\mathbf{C}_{jkpq}\mathbf{G}_{ip,q}(\vec{\mathbf{x}},t;\vec{\xi},\tau)\mathbf{v}_k d\Sigma(\vec{\xi}), \quad (11)$$

in which $\vec{\xi}$ represents points on the crack surface Σ, $\mathbf{G}_{ip,q}$ is the spatial derivative along the direction q of the elastodynamic Green's function at the source location $\vec{\xi}$,$\mathbf{v}_k$ is the kth component of the fault plane's normal unit vector. $[\mathbf{u}_j(\vec{\xi},t)]$ represents the dynamic displacement discontinuity (slip) in the jth direction, in which

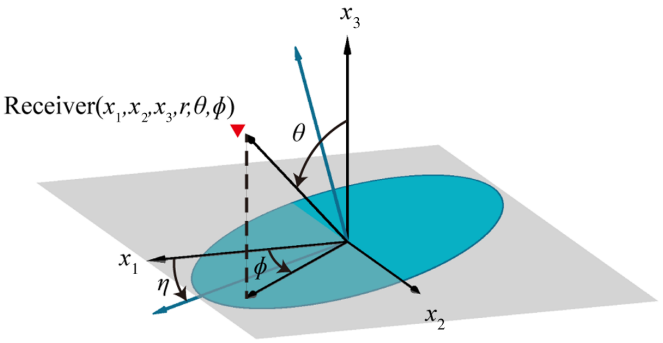

Figure 4. The coordinate system of the kinematic crack model. (x_1, x_2, x_3) is the Cartesian system and (r_0, θ, ϕ) is the spherical coordinates for the receiver location. η is the rotation angle between the crack plane and the x_1 axis. The red triangle indicates the receiver. The color version of this figure is available only in the electronic edition.

$$[\mathbf{u}_j(\vec{\xi},t)] = \mathbf{n}_j\Delta u(\vec{\xi},t), \qquad (12)$$

in which $\Delta u(\vec{\xi},t)$ represents the scalar slip function that can be obtained using equation (10) and n_j represents the jth component of the slip unit vector. The elastodynamic Green's function has been discussed by several researchers (Buchwald, 1959; Ben-Menahem *et al.*, 1991; Gajewski, 1993; Vavryčuk, 1997; Cerveny, 2005; Li and Chesnokov, 2015). Here, we use the Green's function first given by Buchwald (1959), and an efficient way of calculating this Green's function is given by Gajewski (1993). The Green's function is shown as

$$\mathbf{G}_{ip}(\vec{\mathbf{x}},t;\vec{\xi},\tau) = \frac{\mathbf{g}_i\mathbf{g}_p}{4\pi\rho r U\sqrt{|K^{\vec{x}'}|}}\delta(t-\tau-T(\vec{\mathbf{x}},\vec{\xi})), \qquad (13)$$

in which g_k represent the components of the polarization vector, U represents the group velocity, and $K^{\vec{x}'}$ represents the Gaussian curvature of the slowness surface at the source position. The points at which $K^{\vec{x}'}$ equals to zero are named caustics. Equation (13) cannot be used when the receiver is at the caustics. When a ray passes through the caustics, an extra phase shift term is needed for equation (13). For details dealing with caustics, please refer to Chapman (1985), Hanyga and Helle (1995), and Cerveny (2005).

By substituting Green's function (equation 13 into equation 11), we get the formula for far-field body waveform:

$$\mathbf{u}_i(\vec{\mathbf{x}},t) = \frac{1}{4\pi\rho r_0 U\sqrt{|K^{\vec{x}'}|}}\mathbf{g}_i\mathbf{C}_{jkpq}\mathbf{g}_p\mathbf{p}_q\mathbf{v}_k\mathbf{n}_j \iint_{\Sigma}\Delta\dot{u}(\vec{\xi},t-T(\vec{\mathbf{x}},\vec{\mathbf{x}}'))d\Sigma(\vec{\xi}), \qquad (14)$$

in which $\mathbf{p}_i$ are the components of the slowness vector.

We use the expression of the far-field P wave as an example to demonstrate the physical meaning of the first term in equation (14), where the scalar part of the term:

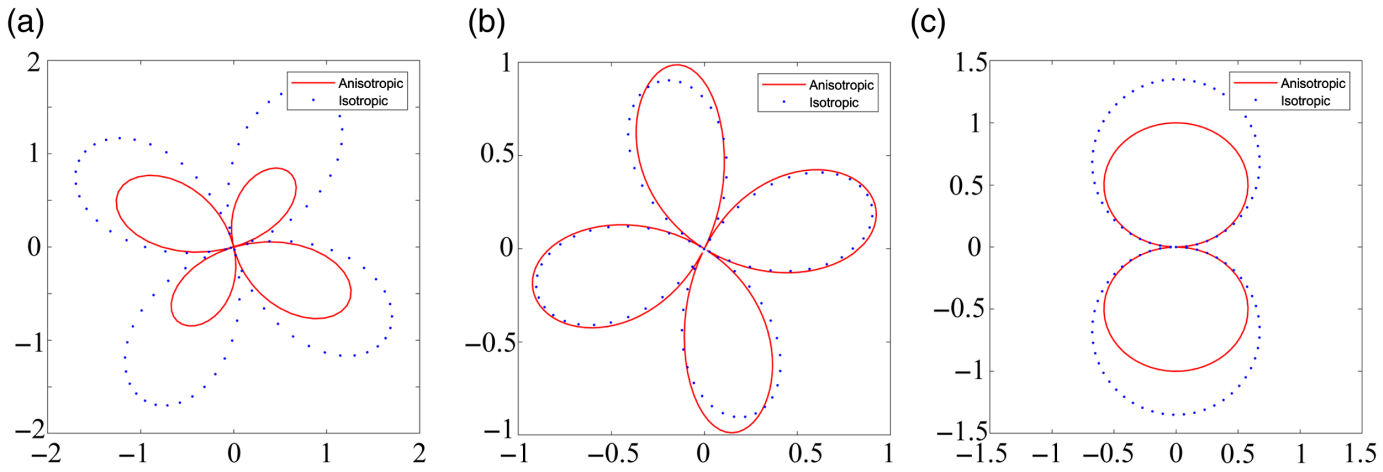

Figure 5. Normalized radiation pattern for quasi *P*, quasi *SV*, and quasi *SH* waves. The radiation patterns of quasi *P* and quasi *SV* are plotted in x_1–x_3 plane whereas the radiation pattern for quasi *SH* is plotted in x_2–x_3 plane. The radiation pattern is normalized by the maximum value of the anisotropic radiation pattern, which could make the axis limits larger than one. (a) Radiation pattern of quasi *P* wave, (b) radiation pattern of quasi *SV* wave, and (c) radiation pattern of quasi *SH* wave. The color version of this figure is available only in the electronic edition.

$$\frac{1}{4\pi\rho r_0 U\sqrt{|K^{\vec{x}}|}}\mathbf{g}_i\mathbf{C}_{jkpq}\mathbf{g}_p\mathbf{p}_q\mathbf{v}_k\mathbf{n}_j, \tag{15}$$

shows the geometric spreading from the source to the receiver and the radiation pattern of the source. The integral part,

$$\Omega(\vec{x},t)\equiv\iint_{\Sigma}\Delta\dot{u}(\vec{\xi},t-T(\vec{\mathbf{x}},\vec{\mathbf{x}}'))d\Sigma(\vec{\xi}), \tag{16}$$

gives the source waveform (which is different from the far-field body waveform).

We calculate radiation patterns and source waveforms using the Mesaverde clayshale (Table 1) as well as a Poisson solid with $V_S = 2074$ m/s as the background medium, the crack rotation angle $\eta = 15°$, the distance between crack the center and receiver $r_0 = 50$ km, and the source function $\Delta u(r,t)$ given by equation (10) with the applied shear stress $\sigma'_{13} = \Delta\sigma = 8.99\times10^5$ Pa, and predefine crack radius R = 2000 m as in the static case.

We show the radiation pattern over the x_1–x_3 plane in Figure 5. Radiation patterns for different sources in different media are widely studied by a lot of researchers (Ben-Menahem and Sena, 1990; Ben-Menahem *et al.*, 1991; Gajewski, 1993; Ben-Menahem and Gibson, 1995). For our calculation, the radiation patterns show similar shape in anisotropic and isotropic media, but the strength of the radiation patterns are different. We also show the source waveforms at several receiver locations shown in Figure 6. The source waveforms of the different locations and different types are shown in Figure 7. The source waveforms in anisotropic and isotropic media share similar shapes. However, there are several differences. One of the differences is that the arrival time for quasi *P*, *SV*, and *SH* waves are different in anisotropic and isotropic media. One noticeable fact is that the differences in quasi *SH* waves are larger than those in quasi *SV* waves. The reason is that the velocity of quasi *SV* wave is controlled by δ and ε (mainly controlled by $\delta-\varepsilon$). At the same time, the velocity of quasi *SH* wave is controlled by γ (Thomsen, 1986; Vavryčuk, 1997). In this Mesaverde shale, the $\delta-\varepsilon$ is small and γ is large. Besides the arrival time, the waveforms in isotropic and anisotropic media have different durations, peak values, and areas of displacement. Those differences show there is an inherent difference between the source waveforms in isotropic and anisotropic. Therefore, ignoring the anisotropic information could cause errors in the inverted stress drop calculated from recorded far-field seismic body waves in practice.

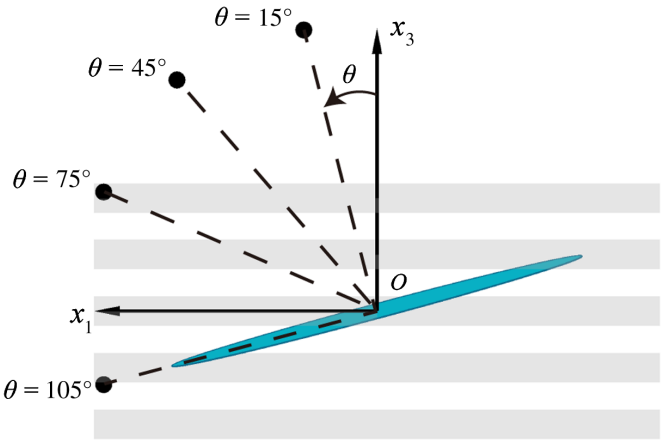

Figure 6. The locations of the source waveform $\Omega(\vec{x},t)$ for the present model for receivers at different θ. This is for the case when the ratio of the rupture velocity and shear velocity is $v/V_S = 0.9$. The color version of this figure is available only in the electronic edition.

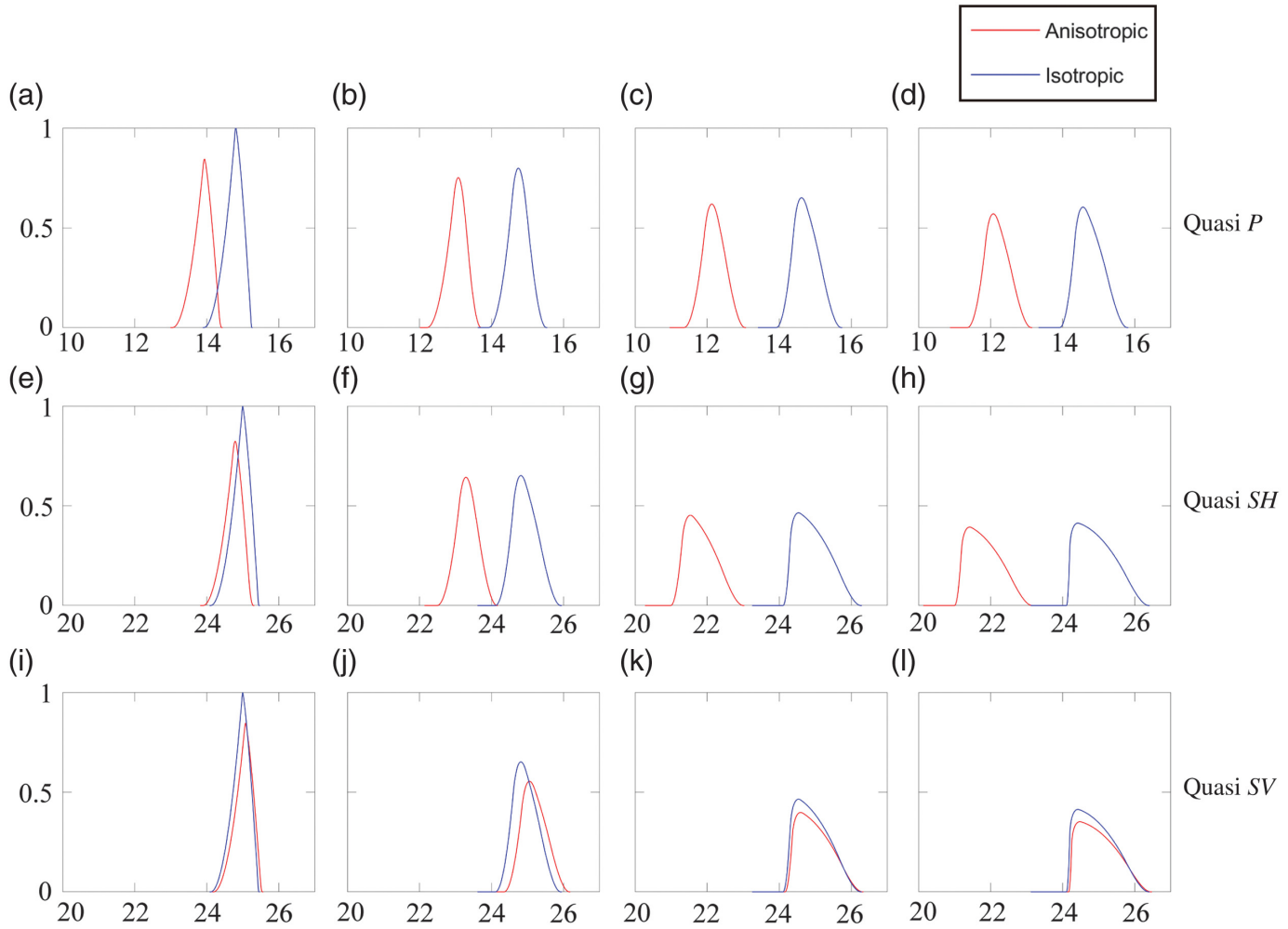

Figure 7. The source waveforms $\Omega(\vec{x}, t)$ for receivers at different θ shown in equation (21). (a–d) Waveforms of the *P* wave, (e–h) waveforms of the *SH* wave, and (i–l) waveforms of the *SV* wave.

Inversion of stress drop

In this section, we describe the steps for calculating stress drop in both isotropic and anisotropic media. Inverting stress drop (both isotropic and anisotropic) involves measuring two properties of the wave spectra. The first property is the long period spectral level ($u(\vec{\mathbf{x}}, \omega \to 0)$), and the second one is the corner frequency. Inverting stress drop in anisotropic media requires the same steps as in isotropic media using just different formulas and constants.

Traditional inversion of stress drop in isotropic media

In isotropic media, we can use long-period spectral level ($u(\vec{\mathbf{x}}, \omega \to 0)$) to estimate the scalar moment M_0 and corner frequency to estimate crack radius R. Then we use the isotropic stress-drop formula equation (9) to invert for the stress drop.

There are several ways to calculate scalar seismic moment; in this article, we discuss the influence of anisotropy on the scalar seismic moment when the moment is calculated from the long-period spectral level. The equation (Aki and Richards, 2002; Kaneko and Shearer, 2014; Clerc *et al.*, 2016) for calculating scalar seismic moment is

$$M_0 = \frac{4\pi\rho V_P^3 r_0 u^P(\vec{\mathbf{x}}, \omega \to 0)}{F^P}, \tag{17}$$

in which $u(\vec{x}, \omega)$ is the spectrum (Fig. 8) of far-field *P*-wave displacement in equation (14) and F^P is the radiation pattern of *P* wave in an isotropic medium, defined as $F^P = 2\gamma_j \mathbf{n}_j \gamma_k \mathbf{v}_k$ (Aki and Richards, 2002). The root mean square value of the radiation pattern on a focal sphere is about 0.52 for *P* wave (0.63 for *S* wave), and the mean absolute value of the radiation pattern is approximately 0.42 for *P* wave (0.59 for *S* wave) according to Kaneko and Shearer (2014). In practice, the stress drop can be usually estimated by averaging the values measured from receivers at different azimuths and takeoff angles to achieve a reliable result (Abercrombie, 2014, 2015; Wu *et al.*, 2018).

The radius of the crack R can be calculated using the measured corner frequency. The corner frequency could be defined by the intersection point between two linear lines in the low- and high-frequency bands. Here, we measure the corner frequency by fitting the normalized spectrum to the ω^{-n} model,

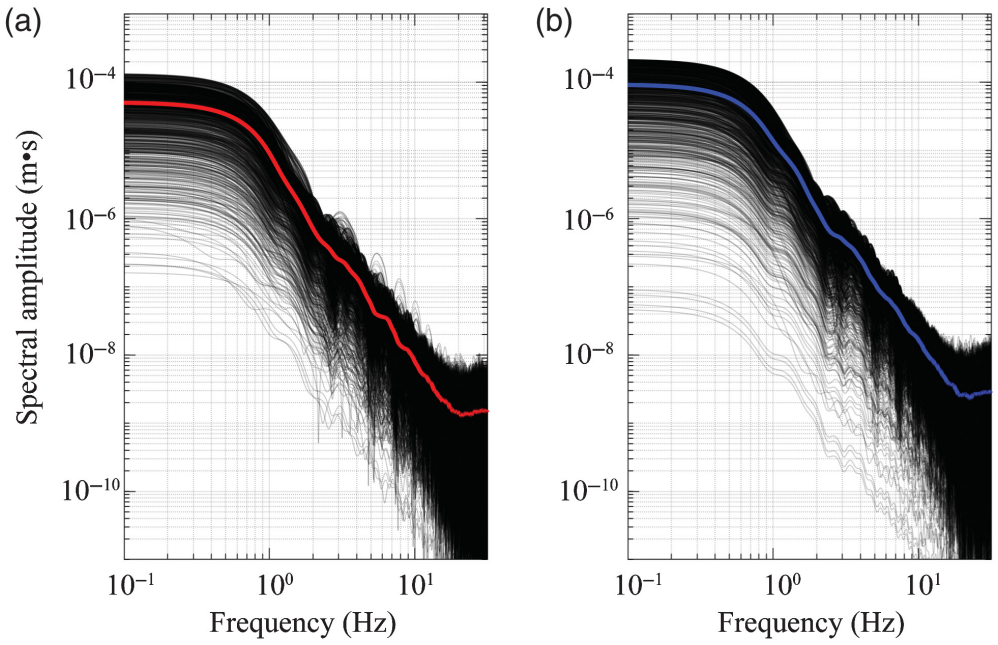

Figure 8. Far-field displacement spectra for receivers uniformly distributed at the sphere with $r_0 = 50$ km. (a) The spectra in the anisotropic media and (b) the spectra in the isotropic media. The colored solid lines are the average spectra for corresponding media.

in which n is the fall-off rate of the high-frequency band, and n is fitted simultaneously with corner frequency. The ω^{-n} model can be described as follows:

$$u(f) = \frac{1}{1 + (f/f_c)^n}, \tag{18}$$

in which $u(f)$ is the spectrum, f is the frequency, and f_c is the corner frequency.

Sato and Hirasawa (1973) gave the relationship between the corner frequency and the radius of the crack in the isotropic medium for both the P and S wave as

$$R = \frac{C_P V_P}{2\pi f_P} = \frac{C_S V_S}{2\pi f_S}, \tag{19}$$

in which C_P and C_S are the model dependent constant, f_P and f_S denote the corner frequency, V_P and V_S are the velocities in isotropic media for P and S wave, respectively. This relationship between the radius of crack and corner frequency is first given by Brune (1970). The constants C_P and C_S could be calculated from synthetic waveform spectra, in which the radius of crack and corner frequencies are known. The C_P and C_S calculated from synthetic data are used to predict the radius of the crack from observed seismic traces. As we stated earlier, instead of using C_P and C_S provided by Sato and Hirasawa (1973), we choose to calculate the corner frequency as well as the C_P and C_S by fitting the spectrum with the ω^{-n} model. Considering the fitting stability, we fit the spectrum using frequencies up to about $10f_c$ similar to Kaneko and Shearer (2015). More details for choosing $10f_c$ can be found in the supplemental material available to this article. The supplemental material includes one figure and one table. Figure S1 shows the differences for the waveforms and frequencies of one receiver with different mesh grids. Table S1 shows the corner frequencies fitted for different fitting ranges and different mesh grids, which impacts our choice of the fitting range. One example of the corner frequencies f_P for receivers around the sphere of 50 km is shown in Figure 9. The parameters are the same as Table 1. The corner frequencies are lower toward the receiver locations that are parallel or perpendicular to the crack surface. The corner frequencies also show less symmetry in the anisotropic medium than in the isotropic medium. The impact of anisotropy on the constants can be found in Appendix D.

Our new inversion of stress drop in anisotropic media

In the anisotropic medium, the scalar seismic moment may not be correctly inverted following the conventional inversion (equation 17). Aki and Richards (2002) proved that the zero frequency of the spectrum is actually equal to the production of the final slip and the fault area ($\Omega(\vec{\mathbf{x}}, \omega \to 0) = A\bar{u}$). We can invert for the $A\overline{u}$ instead of the scalar seismic moment. By removing the effect of the radiation pattern and geometric spreading (equation 15) from the recorded displacement (equation 14), we obtain

$$A\overline{\Delta u} = \Omega(\vec{\mathbf{x}}, \omega \to 0)\frac{4\pi\rho r_0 U\sqrt{|K^{\vec{x}'}|}u^P(\vec{\mathbf{x}}, \omega \to 0)}{\mathbf{g}_i\mathbf{C}_{jkpq}\mathbf{g}_p\mathbf{p}_q\mathbf{v}_k\mathbf{n}_j}. \tag{20}$$

Inserting equation (20) into equation (5), we can calculate the stress drop (shear stress) for the anisotropic medium:

$$\Delta\sigma = -\frac{3}{4}\frac{A\tilde{u}(\tilde{\mathbf{L}}_{3333}\tilde{\mathbf{L}}_{3131} - \tilde{\mathbf{L}}_{3133}\tilde{\mathbf{L}}_{3331})}{\pi R^3\tilde{\mathbf{L}}_{3333}}. \tag{21}$$

Our inversion of stress drop in anisotropic media can be summarized as the following steps:

1. Measure $u^P(\vec{\mathbf{x}}, \omega \to 0)$ and the corner frequency f_c from the recorded waveform.
2. Calculate the R using equation (19) and the production of averaged slip and fault area $A\bar{u}$ using equation (20)
3. Estimate the stress drop $\Delta\sigma$ using equation (21)

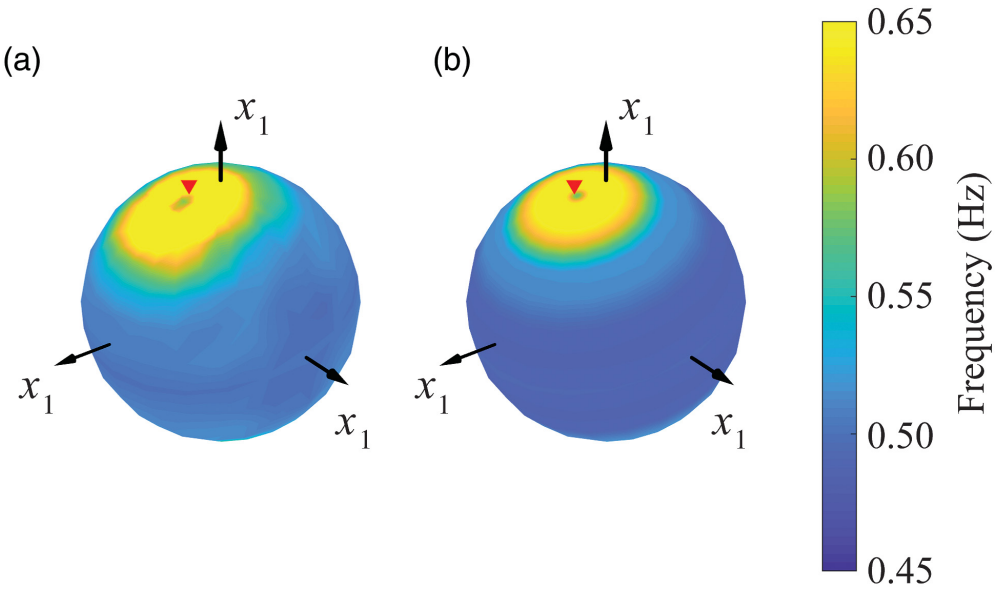

Figure 9. The corner frequencies for the receivers around the sphere with a distance of 50 km. (a) The corner frequencies in an anisotropic medium and (b) the corner frequencies in an isotropic medium. The red angle indicates the point that is perpendicular to the crack surface.

Numerical examples—kinematic inversion of stress drop

In this section, to investigate the effect of anisotropic media on the inversion of stress drop, we design three cases, (1) seismic waveform data from isotropic media and inversion using isotropic stress-drop solution, (2) seismic waveform data from anisotropic media and inversion using isotropic stress-drop solution, and (3) seismic waveform data from anisotropic media and inversion using anisotropic stress-drop solution. We use quasi *P* wave as the example to perform the inversion process, but the principles are the same for quasi *SH* and quasi *SV* waves.

In field data calculation, seismic traces from multireceivers are used to reduce the variance of the receiver's location. In this section, we perform forward modeling using Mesaverde shale (Table 1) as the background medium and set over 1000 receivers (over 200 receivers are used in Tang, 2021) uniformly distributed around the sphere with equal distance (50 km). The average value of the properties over the receivers are used for the inversion calculation. The locations of the receivers are given by the spherical design Womersley (2018).

Case 1: data from isotropic media and inversion using isotropic stress-drop solution. Following the procedure introduced in the Inversion of stress drop section, we first use the spectra of far-field waveforms from isotropic media (Fig. 8a) to estimate the scalar moment M_0 and crack radius R. We then use the isotropic stress-drop equation (9) to invert for the stress drop.

To initialize the inversion, we assume the receivers are located on the sphere with a radius $r_0 = 50$ km. We generate the waveforms in a Poisson's solid medium with density $\rho = 2560$ kg/m^3 and S-wave velocity $V_S = 2074$ m/s, the rupture velocity of the crack equals to 0.9 V_S and the crack has rotation angle $\eta = 15°$. The mean absolute $u(\vec{\mathbf{x}}, \omega \to 0)$ is estimated to be 9.36×10^{-5} m · s (Fig. 8a), and the mean absolute $F^P = 0.42$. Based on equation (17), we obtain $M_0 = 1.64 \times 10^{16}$ N · m.

Next, we estimate the radius of crack. We use the spectra given by Sato and Hirasawa (1973) as the reference spectra for isotropic media. We first infer the reference C_P using the average spectrum, and $C_P = 1.81$ in this situation. Then, we measure the spherical average corner frequency, which is $f_0 = 0.52$ Hz. Thus the calculated radius R is 2 km.

We then use equation (9) to obtain stress drop $\Delta\sigma = 8.99 \times 10^5$ Pa. Compared with the true stress drop $\Delta\sigma = 8.99 \times 10^5$ Pa, the relative misfit is about 1%.

Case 2: data from anisotropic media and inversion using isotropic stress drop solution. In this case, to analyze the error caused by ignoring the anisotropy in an inversion of stress drop, we use the data from anisotropic media to invert for the isotropic stress drop. We generate the waveform using the same geometry of source and receiver as in case 1 but in an anisotropic media. We set the anisotropic background medium with the same properties as Mesaverde clayshale. The inversion procedure is the same as in case 1 although the input data are different. In the spectrum of input data (Fig. 8b), the spectrum at zero frequency is $u(\vec{\mathbf{x}}, \omega \to 0) = 5.1 \times 10^{-5}$ m · s and the corner frequency$f_0 = 0.54$ Hz. Then we obtain $M_0 = 0.90 \times 10^{16}$ N · m using equation (17) Based on the C_P (calculated in case 1) and the measured f_0, we can obatain $R = 1.92$ using equation (19). With equation (9), we obtain the stress drop $\Delta\sigma = 5.50 \times 10^5$ Pa whereas the true shear stress drop is $\Delta\sigma = 8.99 \times 10^5$ Pa. The relative error of inverted stress drop is about 39% if we use isotropic inversion of stress drop but using the data from anisotropic media.

Case 3: data from anisotropic media and anisotropic stress drop solution. Now we use the anisotropic solution

TABLE 2
Inverted Parameters of Three Cases in the Numerical Examples—Kinematic Inversion of Stress Drop Section

Inverted Parameters	Case 1	Case 2	Case 3
Inverted M_0(N · m)	1.64×10^{16}	0.90×10^{16}	
Estimated C_P	1.81	1.81	1.78
Inverted R (km)	2.0	1.92	2.0
Inverted σ (Pa)	8.99×10^5	5.50×10^5	8.99×10^5
Relative error of σ	Less than 1%	39%	Less than 1%

to calculate the stress drop in an anisotropic medium. First, we use equation (20) to calculate the production of the averaged final slip and crack area. In Figure 8b, we can measure the $u(\vec{\mathbf{x}}, \omega \to 0) = 5.1 \times 10^{-5}$ m · s, corner frequency is $f_0 = 0.54$ Hz. We use the true crack radius R to estimate the $C_P = 1.78$.

By using rock parameters of Meversade clayshale, we obtain $A\bar{u} = 1.27 \times 10^6$ m^3 whereas the true model $A\overline{\Delta u} = 1.29 \times 10^6$ m^3. Then we apply equation (21), we obtain the stress drop $\Delta\sigma = 8.99 \times 10^5$ Pa. The relative misfit is less than 1%. We can see that our anisotropic stress drop solution can achieve an accurate inversion of stress drop if we use the correct anisotropy information of the medium.

We summarize the inverted parameters and relative errors of inverted stress strop in Table 2 for these three cases. From Table 2, we can see it is necessary to consider the medium anisotropy in an inversion of stress strop.

In Table 2, we show one example that ignoring anisotropic information will result in a large misfit (39%). In reality, the crack can have different rotation angles, and the slip can point to different directions along the crack surface. In anisotropic media, both the changes of crack orientation and slip direction along the crack will impact the far-field body waveforms. To quantify the impact of those changes, we randomly generate 300 numerical cases with different crack orientations and slip directions along the crack surface. We follow the same procedure as we describe earlier. The results (Fig. 10) show that, in most cases (above 35%), the relative error is about 39%, and there are about 80% of cases have a relative error higher than 38%. The results indicate that the impact of anisotropy should be considered if there is any.

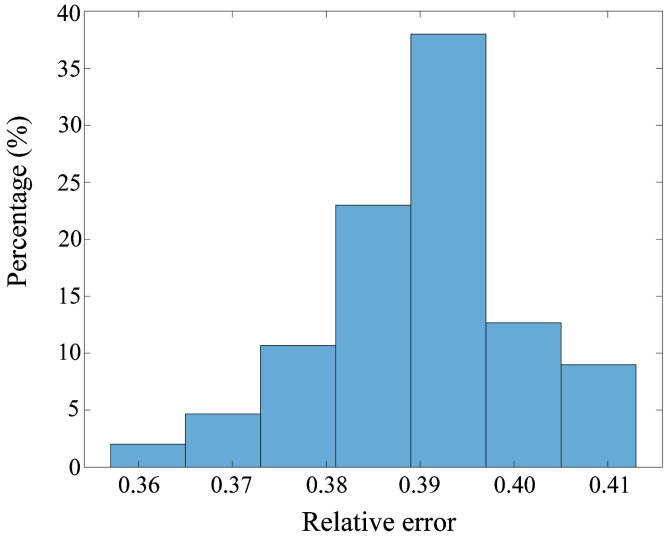

Figure 10. Histogram of the relative errors caused by ignoring anisotropic information. There are 300 cases of inversion with different crack orientations and slip directions along the crack surface. About 80% of the cases have a relative error larger than 38%. The color version of this figure is available only in the electronic edition.

CONCLUSIONS

In this article, we perform theoretical modeling of static and kinematic fault ruptures in both the isotropic and anisotropic media, and analyzed misfit caused by ignoring medium anisotropy. In the static case, we derive the static stress drop formula in anisotropic media. Using this formula, we find that for the same amount of slip, the stress-drop difference can be about 16% between different rotation angles the result shows that, in the anisotropic medium, applying the same stress to cracks with different orientations could produce different magnitudes of slips. One special case is that if the crack is not perpendicular or parallel to the symmetry axis, normal stress can also introduce shear slip that could be up to 10% of the shear slip caused by shear stress.

From the kinematic cases, we derive a simple but compact kinematic modeling formula. Our modeling shows that the constants C_P and C_S will change with different anisotropic parameters. These changes will impact the inferred radius of the crack. We also calculate stress drop using spherical average properties, and the conventional isotopic inversion of stress drop is accurate when the medium is isotropic. However, if the real medium is anisotropic and if one ignores the anisotropy, the inverted stress drop using isotopic formula could have a 39% error in our case. A further study of 300 cases with different crack orientations and slip directions along the crack shows that about 80% of the cases have a relative error higher than 38%, and the largest error is about 41%.

In summary, the anisotropy of background medium could produce a nonnegligible error for the inversion of stress drop in both static solution and kinematic cases. Using our proposed anisotropic stress-drop inversion considering the medium anisotropy, we can correctly invert for the stress drop. To achieve an accurate inversion of stress drop, we suggest the inversion of stress drop should consider the medium anisotropy when it exists.

DATA AND RESOURCES

No data were used in this article. All synthetic data can be provided by request. The supplemental material in this article includes a text, a figure, and a table, which illustrates the details of the authors

choosing the fitting range of the spectrum when calculating corner frequency.

DECLARATION OF COMPETING INTERESTS

The authors acknowledge that there are no conflicts of interest recorded.

ACKNOWLEDGMENTS

The authors would like to thank Jiaxuan Li, Yuandi Gan, David Li, and Yuesu Jin for proofreading. The authors would also like to thank the three anonymous reviewers and the editors from *Bulletin of the Seismological Society of America* for their insightful comments. Yingcai Zheng was partially supported by National Science Foundation (NSF) EAR-2027150 and EAR-1621878.

REFERENCES

Abercrombie, R. E. (2014). Stress drops of repeating earthquakes on the San Andreas Fault at Parkfield, *Geophys. Res. Lett.* **41,** no. 24, 8784–8791.

Abercrombie, R. E. (2015). Investigating uncertainties in empirical green's function analysis of earthquake source parameters, *J. Geophys. Res.* **120,** no. 6, 4263–4277.

Aki, K. (1972). Earthquake mechanism, *Tectonophysics* **13,** nos. 1/4, 423–446.

Aki, K., and P. G. Richards (2002). *Quantitative Seismology*, Second Ed., University Science Books, Mill Valley, California.

Allmann, B. P., and P. M. Shearer (2007). Spatial and temporal stress drop variations in small earthquakes near Parkfield, California, *J. Geophys. Res.* **112,** no. B4, doi: 10.1029/2006JB004395.

Andrews, D. J. (1986). Objective determination of source parameters and similarity of earthquakes of different size, in *Earthquake Source Mechanics*, S. Das, J. Boatwright, and C. H. Scholz (Editors), Vol. 37, American Geophysical Union, Washington D.C., 259–267.

Baltay, A. S., T. C. Hanks, and G. C. Beroza (2013). Stable stress-drop measurements and their variability: Implications for ground-motion prediction, *Bull. Seismol. Soc. Am.* **103,** no. 1, 211–222.

Ben-Menahem, A., and R. L. Gibson Jr. (1995). Radiation of elastic waves from sources embedded in anisotropic inclusions, *Geophys. J. Int.* **122,** no. 1, 249–265.

Ben-Menahem, A., and A. G. Sena (1990). Seismic source theory in stratified anisotropic media, *J. Geophys. Res.* **95,** no. B10, 15,395–15,427.

Ben-Menahem, A., R. L. Gibson Jr., and A. G. Sena (1991). Green's tensor and radiation patterns of point sources in general anisotropic inhomogeneous elastic media, *Geophys. J. Int.* **107,** no. 2, 297-308.

Boatwright, J. (1980). A spectral theory for circular seismic sources; simple estimates of source dimension, dynamic stress drop, and radiated seismic energy, *Bull. Seismol. Soc. Am.* **70,** no. 1, 1–27.

Brune, J. N. (1970). Tectonic stress and the spectra of seismic shear waves from earthquakes, *J. Geophys. Res.* **75,** no. 26, 4997–5009.

Buchwald, V. T. (1959). Elastic waves in anisotropic media, *Proc. Math. Phys. Sci.* **253,** no. 1275, 563–580.

Cerveny, V. (2005). *Seismic Ray Theory*, Cambridge University Press, New York, New York.

Chapman, C. (1985). Ray theory and its extensions: WKBJ and Maslov seismograms, *J. Geophys.* **58,** no. 1, 27–43.

Clerc, F., R. M. Harrington, Y. Liu, and J. G. Yu (2016). Stress drop estimates and hypocenter relocations of induced seismicity near crooked lake, Alberta: Stress drops of the CLS, *Geophys. Res. Lett.* **43,** no. 13, 6942–6951.

Cocco, M., E. Tinti, and A. Cirella (2016). On the scale dependence of earthquake stress drop, *J. Seismol.* **20,** no. 4, 1151–1170.

Dahlen, F. (1974). On the ratio of P-wave to S-wave corner frequencies for shallow earthquake sources, *Bull. Seismol. Soc. Am.* **64,** no. 4, 1159–1180.

Dong, G., and A. S. Papageorgiou (2002a). Seismic radiation from a unidirectional asymmetrical circular crack model, part I: Constant rupture velocity, *Bull. Seismol. Soc. Am.* **92,** no. 3, 945–961.

Dong, G., and A. S. Papageorgiou (2002b). Seismic radiation from a unidirectional asymmetrical circular crack model, part II: Variable rupture velocity, *Bull. Seismol. Soc. Am.* **92,** no. 3, 962–982.

Eshelby, J. D. (1957). The determination of the elastic field of an ellipsoidal inclusion, and related problems, *Proc. Math. Phys. Sci.* **241,** no. 1226, 376–396.

Gajewski, D. (1993). Radiation from point sources in general anisotropic media, *Geophys. J. Int.* **113,** no. 2, 299–317.

Goertz-Allmann, B. P., A. Goertz, and S. Wiemer (2011). Stress drop variations of induced earthquakes at the Basel geothermal site, *Geophys. Res. Lett.* **38,** no. 9, doi: 10.1029/2011GL047498.

Grechka, V., and S. Yaskevich (2013). Azimuthal anisotropy in microseismic monitoring: A Bakken case study, *Geophysics* **79,** no. 1, KS1–KS12.

Hanks, T. C., and R. K. Mcguire (1981). The character of high-frequency strong ground motion, *Bull. Seismol. Soc. Am.* **71,** no. 3, 1897–1919.

Hanyga, A., and H. B. Helle (1995). Synthetic seismograms from generalized ray tracing 1, *Geophys. Prospect.* **43,** no. 1, 51–75.

Huang, Y., G. C. Beroza, and W. L. Ellsworth (2016). Stress drop estimates of potentially induced earthquakes in the guy-greenbrier sequence, *J. Geophys. Res.* **121,** no. 9, 6597–6607.

Hutchings, L. (1994). Kinematic earthquake models and synthesized ground motion using empirical green's functions, *Bull. Seismol. Soc. Am.* **84,** no. 4, 1028–1050.

Kanamori, H., and D. L. Anderson (1975). Theoretical basis of some empirical relations in seismology, *Bull. Seismol. Soc. Am.* **65,** no. 5, 1073–1095.

Kanamori, H., and E. Brodsky (2004). The physics of earthquakes, *Rep. Prog. Phys.* **67,** no. 8, 1429.

Kaneko, Y., and P. M. Shearer (2014). Seismic source spectra and estimated stress drop derived from cohesive-zone models of circular subshear rupture, *Geophys. J. Int.* **197,** no. 2, 1002–1015.

Kaneko, Y., and P. M. Shearer (2015). Variability of seismic source spectra, estimated stress drop, and radiated energy, derived from cohesive-zone models of symmetrical and asymmetrical circular and elliptical ruptures, *J. Geophys. Res.* **120,** no. 2, 1053–1079.

Li, Z., and E. M. Chesnokov (2015). Elastodynamic Green's tensor in vertically transversely isotropic media, *J. Seismic Explor.* **24,** no. 3, 259–280.

Li, J., Y. Zheng, L. Thomsen, T. J. Lapen, and X. Fang (2018). Deep earthquakes in subducting slabs hosted in highly anisotropic rock fabric, *Nature Geosci.* **11,** no. 9, 696.

Lin, Y.-Y., K.-F. Ma, and V. Oye (2012). Observation and scaling of microearthquakes from the Taiwan Chelungpu-fault borehole seismometers, *Geophys. J. Int.* **190,** no. 1, 665–676.

Madariaga, R. (1976). Dynamics of an expanding circular fault, *Bull. Seismol. Soc. Am.* **66,** no. 3, 639–666.

Mavroeidis, G. P., B. Zhang, G. Dong, A. S. Papageorgiou, U. Dutta, and N. N. Biswas (2008). Estimation of strong ground motion from the great 1964 Mw 9.2 Prince William Sound, Alaska, earthquake estimation of strong ground motion from the great 1964 Prince William Sound, Alaska, earthquake, *Bull. Seismol. Soc. Am.* **98,** no. 5, 2303-2324.

Mura, T. (1987). *Micromechanics of Defects in Solids*, Kluwer Academic Publishers, Dordrecht, The Netherlands.

Oncescu, M. C. (1986). Some source and medium properties of the Vrancea seismic region, Romania, *Tectonophysics* **126,** nos. 2/4, 245–258.

Sato, T., and T. Hirasawa (1973). Body wave spectra from propagating shear cracks, *J. Phys. Earth* **21,** no. 4, 415–431.

Sato, T., and T. Hirasawa (2009). Seismic radiation from circular cracks growing at variable rupture velocity, *Bull. Seismol. Soc. Am.* **84,** no. 4, 1199–1215.

Schoenberg, M., and C. M. Sayers (1995). Seismic anisotropy of fractured rock, *Geophysics* **60,** no. 1, 204–211.

Snoke, J. A. (1987). Stable determination of (Brune) stress drops, *Bull. Seismol. Soc. Am.* **77,** no. 2, 530–538.

Sondergeld, C. H., and C. S. Rai (2011). Elastic anisotropy of shales, *The Leading Edge* **30,** no. 3, 324–331.

Song, T. R. A., and H. Kawakatsu (2012). Subduction of oceanic asthenosphere: Evidence from sub-slab seismic anisotropy, *Geophys. Res. Lett.* **39,** no. 17, doi: 10.1029/2012GL052639.

Talebi, S., and T. J. Boone (1998). Source parameters of injection-induced microseismicity, *Pure Appl. Geophys.* **153,** no. 1, 113–130.

Tang, S. (2021). Reconstruction of sparsely sampled seismic data via residual u-net and earthquake stress drop for a circular crack in an anisotropic medium, *Ph.D. Dissertation*, University of Houston, Houston, Texas.

Thomsen, L. (1986). Weak elastic anisotropy, *Geophysics* **51,** no. 10, 1954–1966.

Uchida, N., T. Matsuzawa, W. L. Ellsworth, K. Imanishi, K. Shimamura, and A. Hasegawa (2012). Source parameters of microearthquakes on an interplate asperity off Kamaishi, ne Japan over two earthquake cycles, *Geophys. J. Int.* **189,** no. 2, 999-1014.

Udias, A., R. Madariaga, and E. Buforn (2014). *Source Mechanisms of Earthquakes: Theory and Practice*, Cambridge University Press, New York, New York.

Vavryčuk, V. (1997). Elastodynamic and elastostatic green tensors for homogeneous weak transversely isotropic media, *Geophys. J. Int.* **130,** no. 3, 786–800.

Walpole, L. (1977). The determination of the elastic field of an ellipsoidal inclusion in an anisotropic medium, *Proc of the Mathematical Proceedings of the Cambridge Philosophical Society*, Vol. 81, Cambridge University Press, 283–289.

Weinberger, C., C. Wei, and D. Barnett (2005). Lecture notes—Elasticity of microscopic structures, available at http://micro.stanford.edu/~caiwei/me340b/content/me340b-notes_v01.pdf (last accessed September 2005).

Womersley, R. S. (2018). *Efficient Spherical Designs with Good Geometric Properties*, Springer, Cham, Switzerland.

Wu, Q., M. Chapman, and X. Chen (2018). Stress-drop variations of induced earthquakes in Oklahoma, *Bull. Seismol. Soc. Am.* **108,** no. 3A, 1107–1123.

Zollo, A., A. Orefice, and V. Convertito (2014). Source parameter scaling and radiation efficiency of microearthquakes along the Irpinia fault zone in southern Apennines, Italy, *J. Geophys. Res.* **119,** no. 4, 3256–3275.

APPENDIX A

The slip (displacement discontinuity) can be expressed as follows:

$$\mathbf{u}_1(\mathbf{x}_3) = 2\mathbf{e}^*_{13}\mathbf{x}_3 = \frac{1}{2}\Delta u(\mathbf{x}_1, \mathbf{x}_2, \mathbf{x}_3), \tag{A1}$$

in which $\mathbf{u}_1$ measures displacement along the x_1 direction and $\mathbf{e}^*_{13}$ is the eigenstrain. Because the crack is an ellipsoid, its boundary is defined by

$$\frac{\mathbf{x}_1^2}{a_1^2} + \frac{\mathbf{x}_2^2}{a_2^2} + \frac{\mathbf{x}_3^2}{a_3^2} = 1, \tag{A2}$$

and the slip on the crack surface is

$$\Delta u(\mathbf{x}_1, \mathbf{x}_2, \mathbf{x}_3) = 4(\mathbf{e}^*_{13}a_3)\frac{\mathbf{x}_3}{a_3} = 4(\mathbf{e}^*_{13}a_3)\sqrt{1 - \left(\frac{\mathbf{x}_1}{a_1}\right)^2 - \left(\frac{\mathbf{x}_2}{a_2}\right)^2}. \tag{A3}$$

We further assume that $a_1 = a_2 = R$ and we can rewrite equation (A3) as

$$\Delta u(r) = 4(\mathbf{e}^*_{13}a_3)\sqrt{1 - \frac{r^2}{R^2}}, \tag{A4}$$

in which $r = \sqrt{\mathbf{x}_1^2 + \mathbf{x}_2^2}$. The eigenstrain $\mathbf{e}^*_{13}$ in a general anisotropic medium is given by Mura (1987) as

$$a_3\mathbf{e}^*_{13} = -\frac{\mathbf{L}_{3333}}{2(\mathbf{L}_{3333}\mathbf{L}_{3131} - \mathbf{L}_{3133}\mathbf{L}_{3331})}\sigma_{13}, \tag{A5}$$

in which a_3 is assumed to be approaching zero, that is, $a_3 \to 0$. In equation (A5), the tensor $\mathbf{L}_{ijmn}$ is defined as

$$\mathbf{L}_{ijmn} = -\frac{1}{4\pi}\mathbf{C}_{ijkl}\mathbf{C}_{pqmn}\Pi_{kplq}, \tag{A6}$$

in which $\mathbf{C}_{ijkl}$ is the fourth-rank elastic stiffness tensor and each subscript takes value 1, 2, or 3, and

$$\Pi_{kplq} = \int_{S^2} \frac{\mathbf{G}_{kplq}(\vec{\xi})dS(\vec{\xi})}{a_1^2a_2^2a_3^2\left(\frac{\vec{\xi}_1^2}{a_2^2a_3^2} + \frac{\vec{\xi}_2^2}{a_3^2a_1^2} + \frac{\vec{\xi}_3^2}{a_1^2a_2^2}\right)^{\frac{3}{2}}}, \tag{A7}$$

in which $\mathbf{G}_{kplq}$ is a tensor in a homogeneous anisotropic medium given by Mura (1987) and the $\vec{\xi}$ is the directional vector lies on a unit sphere. $\mathbf{G}_{kplq}$ is given as

$$\mathbf{G}_{kplq}(\xi) = \mathbf{N}_{kp}(\xi)\xi_l\xi_q/D(\xi), \tag{A8}$$

in which $\mathbf{N}_{ij}(\xi)$ and $D(\xi)$ are the cofactor and the determinant of the matrix $\mathbf{K}_{ki} = \mathbf{C}_{kjil}\xi_j\xi_l$, respectively, in which $\mathbf{C}_{kjil}$, ξ_i are the coordinates of ξ, the index k, j, i, l run over 1, 2, 3.

Because we assume $a_1 = a_2 = R$, the tensor $\mathbf{L}_{ijmn}$ is a linear function of $\frac{1}{R}$. To emphasize this fact, we write $\mathbf{L}_{ijmn} = \frac{1}{R}\tilde{\mathbf{L}}_{ijmn}$ in the following equations.

Inserting equation (A5) into equation (A4), we obtain

$$\Delta u(r) = \frac{-2\sigma_{13}\tilde{\mathbf{L}}_{3333}}{\tilde{\mathbf{L}}_{3333}\tilde{\mathbf{L}}_{3131} - \tilde{\mathbf{L}}_{3133}\tilde{\mathbf{L}}_{3331}}\sqrt{R^2 - r^2}. \tag{A9}$$

APPENDIX B

In isotropic media, equations (2) and (3) can be calculated analytically. Here we give the analytical result. To make the forms more compact, we follow the Voigt recipe to write Π_{kplq} as $\mathbf{\Pi}_{\alpha\beta}$ and $\tilde{\mathbf{L}}_{ijmn}$ as $\tilde{\mathbf{L}}_{\alpha\beta}$, in which α and β range from 1 to 6. The change in indices is given as follows:

$$\begin{array}{ccccccccccccc} ij & or & kl & : & 11 & 22 & 33 & 32=23 & 31=13 & 12=21 \\ \downarrow & & \downarrow & & \downarrow & \downarrow & \downarrow & \downarrow & \downarrow & \downarrow \\ \alpha & & \beta & & 1 & 2 & 3 & 4 & 5 & 6 \end{array}. \tag{B1}$$

The $\mathbf{\Pi}_{\alpha\beta}$, which are not zero, are listed subsequently:

$$\begin{aligned}
\mathbf{\Pi}_{11} &= -\frac{5\pi^2}{8\mu R} - \frac{3\pi^2}{8(\lambda+2\mu)R} \\
\mathbf{\Pi}_{12} = \mathbf{\Pi}_{21} &= -\frac{7\pi^2}{8\mu R} - \frac{\pi^2}{8(\lambda+2\mu)R} \\
\mathbf{\Pi}_{13} = \mathbf{\Pi}_{23} &= \frac{5\pi^2}{2\mu R} - \frac{\pi^2}{2(\lambda+2\mu)R} \\
\mathbf{\Pi}_{22} &= -\frac{5\pi^2}{8\mu R} - \frac{3\pi^2}{8(\lambda+2\mu)R} \\
\mathbf{\Pi}_{31} = \mathbf{\Pi}_{32} &= -\frac{(\lambda+3\mu)\pi^2}{2\mu(\lambda+2\mu)R} \\
\mathbf{\Pi}_{33} &= -\frac{(\lambda-\mu)\pi^2}{\mu(\lambda+2\mu)R} \\
\mathbf{\Pi}_{44} = \mathbf{\Pi}_{55} &= \frac{(\lambda+\mu)\pi^2}{2\mu(\lambda+2\mu)R} \\
\mathbf{\Pi}_{66} &= \frac{(\lambda+\mu)\pi^2}{8\mu(\lambda+2\mu)R}.
\end{aligned} \tag{B2}$$

The $\tilde{\mathbf{L}}_{\alpha\beta}$ are listed as well:

$$\begin{aligned}
\mathbf{L}_{11} &= \frac{13\pi\mu(\lambda+\mu)}{8(\lambda+2\mu)}, \\
\tilde{\mathbf{L}}_{12} = \tilde{\mathbf{L}}_{21} &= \frac{\pi\mu(7\lambda-\mu)}{8(\lambda+2\mu)}, \\
\tilde{\mathbf{L}}_{13} = \tilde{\mathbf{L}}_{23} &= -\frac{\pi\mu(2\lambda+\mu)}{2(\lambda+2\mu)}, \\
\tilde{\mathbf{L}}_{22} &= \frac{13\pi\mu(\lambda+\mu)}{8(\lambda+2\mu)}, \\
\tilde{\mathbf{L}}_{31} = \tilde{\mathbf{L}}_{32} &= -\frac{\pi\mu(2\lambda+\mu)}{2(\lambda+2\mu)}, \\
\tilde{\mathbf{L}}_{33} &= -\frac{\pi\mu(\lambda+\mu)}{(\lambda+2\mu)}, \\
\tilde{\mathbf{L}}_{44} = \tilde{\mathbf{L}}_{55} &= -\frac{\pi\mu(3\lambda+4\mu)}{4(\lambda+2\mu)}, \\
\tilde{\mathbf{L}}_{66} &= \frac{\pi\mu(3\lambda+7\mu)}{8(\lambda+2\mu)}.
\end{aligned} \tag{B3}$$

APPENDIX C

In this appendix, we give the relationship between Thomsen parameters and the elastic modulus. The Thomsen parameters are widely used because the parameters can be grasped intuitively. The Thomsen parameters are used for transverse isotropy media:

$$\mathbf{C}_{\alpha\beta} = \begin{bmatrix} \mathbf{C}_{11} & (\mathbf{C}_{11}-2\mathbf{C}_{66}) & \mathbf{C}_{13} & & & \\ (\mathbf{C}_{11}-2\mathbf{C}_{66}) & \mathbf{C}_{11} & \mathbf{C}_{13} & & & \\ \mathbf{C}_{13} & \mathbf{C}_{13} & \mathbf{C}_{33} & & & \\ & & & \mathbf{C}_{44} & & \\ & & & & \mathbf{C}_{44} & \\ & & & & & \mathbf{C}_{66} \end{bmatrix}. \tag{C1}$$

Then the parameters are given as

$$V_P = \sqrt{\mathbf{C}_{33}/\rho}, \tag{C2}$$

$$V_S = \sqrt{\mathbf{C}_{44}/\rho}, \tag{C3}$$

$$\varepsilon = \frac{\mathbf{C}_{11} - \mathbf{C}_{33}}{2\mathbf{C}_{33}}, \tag{C4}$$

$$\gamma = \frac{\mathbf{C}_{66} - \mathbf{C}_{44}}{2\mathbf{C}_{44}}, \tag{C5}$$

and

$$\delta = \frac{(\mathbf{C}_{13}+\mathbf{C}_{44})^2 - (\mathbf{C}_{33}-\mathbf{C}_{44})^2}{2\mathbf{C}_{33}(\mathbf{C}_{33}-\mathbf{C}_{44})}. \tag{C6}$$

Equation (C4) shows that the parameter ε reflects the difference between vertical and horizontal P velocities; equation (C5) shows that the parameter γ reflects the difference between

vertical and horizontal *SH* velocities; the parameter δ involves the anisotropy of both quasi *P* and quasi *S* waves.

From equation (C4) to (C6) the elastic modulus can be calculate by Thomsen parameters as

$$\mathbf{C}_{11} = 2\varepsilon\mathbf{C}_{33} + \mathbf{C}_{33}, \tag{C7}$$

$$\mathbf{C}_{66} = 2\gamma\mathbf{C}_{44} + \mathbf{C}_{44}, \tag{C8}$$

$$\mathbf{C}_{13} = \sqrt{2\delta\mathbf{C}_{33}(\mathbf{C}_{33} - \mathbf{C}_{44}) + (\mathbf{C}_{33} - \mathbf{C}_{44})^2} - \mathbf{C}_{44}. \tag{C9}$$

TABLE D1
C_P with Different ε and δ by the Fitting Method

Anisotropic Parameters	$\varepsilon = 0$	$\varepsilon = 0.05$	$\varepsilon = 0.1$	$\varepsilon = 0.15$	$\varepsilon = 0.2$
$\delta = 0$	1.73	1.73	1.75	1.76	1.77
$\delta = 0.05$	1.73	1.74	1.75	1.76	1.77
$\delta = 0.1$	1.74	1.75	1.76	1.77	1.78
$\delta = 0.15$	1.74	1.75	1.76	1.77	1.78
$\delta = 0.2$	1.74	1.75	1.77	1.78	1.79

TABLE D2
C_P with Different ε and δ by Andrews' Definition

Anisotropic Parameters	$\varepsilon = 0$	$\varepsilon = 0.05$	$\varepsilon = 0.1$	$\varepsilon = 0.15$	$\varepsilon = 0.2$
$\delta = 0$	1.24	1.25	1.26	1.27	1.28
$\delta = 0.05$	1.24	1.25	1.26	1.27	1.28
$\delta = 0.1$	1.25	1.26	1.27	1.27	1.28
$\delta = 0.15$	1.25	1.26	1.27	1.28	1.28
$\delta = 0.2$	1.25	1.26	1.27	1.28	1.29

TABLE D3
C_P with Different ε and δ by Snoke's Definition

Anisotropic Parameters	$\varepsilon = 0$	$\varepsilon = 0.05$	$\varepsilon = 0.1$	$\varepsilon = 0.15$	$\varepsilon = 0.2$
$\delta = 0$	1.44	1.46	1.47	1.48	1.49
$\delta = 0.05$	1.45	1.46	1.47	1.48	1.49
$\delta = 0.1$	1.45	1.46	1.48	1.49	1.50
$\delta = 0.15$	1.45	1.47	1.48	1.49	1.50
$\delta = 0.2$	1.45	1.47	1.48	1.49	1.50

From Tables D1 to D3, we can see that the trends of C_P in different methods are similar and the values of C_P are increasing with the anisotropic parameters increasing. Since we fixed the ratio of rupture velocity with V_S (not V_P), the C_P for the Poisson solid is different from the C_P in isotropic media. We calculate the values of C_P in the Poisson solid for comparison. For a Poisson solid, the C_P by fitting is 1.80; the definition of Andrews (1986) and Snoke (1987) are 1.53 and 1.72, respectively. The C_P values, given by Sato and Hirasawa (1973), Madariaga (1976), and Kaneko and Shearer (2015) are 1.60, 1.16, and 1.38, respectively. Then we discuss the impact of anisotropy on the constant C_{SV} and C_{SH}. In VTI media, C_{SV} depends on the subtraction of ε and δ, and C_{SH} depends on the parameter γ. We also limited the range of the parameters $(\varepsilon - \delta, \gamma)$ from 0 to 0.2. The result is listed in Tables D4 and D5. When the $\varepsilon - \delta = 0.2$, there is a travel-time triplication for the *SV* wave. The corner frequencies are not calculated in this situation. VTI, vertical transversely isotropic.

APPENDIX D

In this appendix, we discuss the effects of anisotropy on the corner frequency and its related constants (C_P and C_S) using the same geometric setting as in Numerical Examples—Kinematic Inversion of Stress Drop section. There are several ways to measure the corner frequency. Sato and Hirasawa (1973) use graphic picking as the tool to measure the corner frequency. However, manually picking could be labor intensive. Instead of manually picking, fitting a ω^{-n} spectrum can

TABLE D4
C_{SV} with Different $\varepsilon - \delta$ for All Three Methods

Calculation Methods	0	0.05	0.1	0.15	0.2
Fitting	2.71	2.64	2.59	2.57	Travel-time triplication
Andrews	2.39	2.43	2.47	2.50	Travel-time triplication
Snoke	2.48	2.49	2.51	2.53	Travel-time triplication

TABLE D5
C_{SH} with Different γ for All Three Methods

Calculation Methods	0	0.05	0.1	0.15	0.2
Fitting	2.71	2.91	2.96	2.90	2.80
Andrews	2.39	2.30	2.26	2.23	2.17
Snoke	2.48	2.44	2.42	2.39	2.34

In anisotropic media, even if the anisotropic parameters do not change, the variance of the crack orientation can still change the constants C_P, C_{SV}, and C_{SH}. We use the anisotropic parameters of Mervasade sandstone as an example to show the impact of angle η to the constants C_P, C_{SV}, and C_{SH}, and the results are listed in Tables D6–D8. The trends of C_P, C_{SV}, and C_{SH} values are not monotonic with the increasing angle η, which could be because of the fitting instability or the complex relationship between the C_P/C_S and angle η.

TABLE D6
C_P with Different η Angles for Mesaverde Sandstone for All Three Methods

Calculation Methods	0	15	30	45	60	75	90
Fitting	1.79	1.78	1.76	1.75	1.73	1.72	1.72
Andrews	1.29	1.28	1.27	1.26	1.25	1.24	1.24
Snoke	1.50	1.50	1.48	1.47	1.45	1.44	1.44

TABLE D7
C_{SV} with Different η Angles for Mesaverde Sandstone for All Three Methods

Calculation Methods	0	15	30	45	60	75	90
Fitting	2.70	2.68	2.65	2.61	2.57	2.54	2.54
Andrews	2.41	2.41	2.44	2.47	2.52	2.58	2.60
Snoke	2.49	2.49	2.50	2.51	2.54	2.57	2.58

TABLE D8
C_{SH} with Different η Angles for Mesaverde Sandstone for All Three Methods

Calculation Methods	0	15	30	45	60	75	90
Fitting	2.84	2.85	2.83	2.73	2.53	2.42	2.43
Andrews	2.21	2.21	2.23	2.27	2.42	2.51	2.44
Snoke	2.37	2.37	2.37	2.38	2.45	2.49	2.44

be more computationally efficient. Besides those two methods, there are also other methods calculating corner frequency based on different definitions that could be more objective.

In this appendix, we calculate the three types of measured corner frequency, by fitting ω^{-n} spectra, the definition of Andrews, and the definition of Snoke (1987). In addition, the measured corner frequencies are averaged from over 1000 receivers on the sphere with equal distance (Womersley, 2018). Based on the spherical average corner frequencies, we obtain the constants (e.g., C_P and C_S) (equation 19) for different anisotropy parameters δ, ε, and γ. In all the calculations, we fix $v/V_S = 0.9$ as we describe before. Fixing the rupture velocity with shear velocity will make the phenomena that C_P in isotropic media and the Poisson solid yield different values, whereas C_S yield the same value in both media.

First, we discuss the impact of anisotropy on the constant C_P. In vertical transversely isotropic media, the P wave depends on two factors δ and ε. Here, we only consider the anisotropic parameters in the range 0–0.2. The calculated C_P values are given in Tables D1–D3.

Manuscript received 3 May 2022
Published online 15 November 2022